Geophysical Research Letters

RESEARCH LETTER
10.1029/2023GL107788

Key Points:

- We map the 3D displacements, slip distribution, and stress fields related to the 2023 Turkey-Syria Earthquake doublet
- Dramatic stress rotation occurred after the Earthquake doublet, up to 29°
- Stress rotation and horsetail splay fault structure are potentially responsible for normal-faulting aftershocks

Supporting Information:

Supporting Information may be found in the online version of this article.

Correspondence to:

S. Wei,
shjwei@ntu.edu.sg

Citation:

Ma, Z., Li, C., Jiang, Y., Chen, Y., Yin, X., Aoki, Y., et al. (2024). Space geodetic insights to the dramatic stress rotation induced by the February 2023 Turkey-Syria earthquake doublet. *Geophysical Research Letters*, *51*, e2023GL107788. https://doi.org/10.1029/2023GL107788

Received 10 DEC 2023
Accepted 23 JAN 2024

Author Contributions:

Conceptualization: Zhangfeng Ma, Yukuan Chen, Xinzhong Yin, Sang-Ho Yun, Shengji Wei
Data curation: Zhangfeng Ma, Chenglong Li
Formal analysis: Zhangfeng Ma, Yu Jiang, Yukuan Chen, Shengji Wei
Funding acquisition: Shengji Wei
Investigation: Zhangfeng Ma, Shengji Wei
Methodology: Zhangfeng Ma, Chenglong Li, Yu Jiang
Resources: Zhangfeng Ma
Software: Zhangfeng Ma
Supervision: Yosuke Aoki, Sang-Ho Yun, Shengji Wei
Validation: Zhangfeng Ma
Visualization: Zhangfeng Ma

Space Geodetic Insights to the Dramatic Stress Rotation Induced by the February 2023 Turkey-Syria Earthquake Doublet

Zhangfeng Ma[1], Chenglong Li[1,2], Yu Jiang[1], Yukuan Chen[1], Xinzhong Yin[1,2], Yosuke Aoki[3], Sang-Ho Yun[1,4,5], and Shengji Wei[1,4]

[1]Earth Observatory of Singapore, Singapore, Singapore, [2]Institute of Geology, China Earthquake Administration, Beijing, China, [3]Earthquake Research Institute, The University of Tokyo, Tokyo, Japan, [4]Asian School of the Environment, Nanyang Technological University, Singapore, Singapore, [5]School of Electrical and Electronic Engineering, Nanyang Technological University, Singapore, Singapore

Abstract The February 2023 Turkey-Syria Earthquake doublet ruptured multiple segments of the East Anatolian Fault (EAF) Zone. Dominating seismicity focal mechanism shifted dramatically from strike-slip to normal-faulting after the doublet. To better understand this shift, here we derived a comprehensive 3D co-seismic displacement field and performed the stress analysis. Abundant space geodetic data were used to generate high-resolution 3D surface displacement, which provide tight constraints on fault geometry, slip distribution and stress field. Together with stress inversion from aftershock focal mechanisms, we show that the principal stress direction rotation in the region with the most normal-faulting aftershocks is the staggering 29°. The induced heterogenous stress may explain the shift of the dominant focal mechanism toward normal faulting. We suggest that the extensional horsetail splay faults, likely formed through geologic time scale related to the releasing bend on the EAF, are the hosts of most of the normal faulting aftershocks.

Plain Language Summary Sudden dislocation of two sides of a fault, or the rupture of rocks, produces an earthquake. The dislocation direction relative to the fault traces reflects the direction of stress that are responsible for the earthquake. When dislocation direction is parallel to the fault strike, the earthquake is termed as strike-slip type, and termed as normal-faulting type when they are perpendicular. A remarkable feature for the 2023 Turkey-Syria Mw7.8 & 7.7 earthquake doublet is that, background seismicity shifted dramatically from strike-slip to normal type of faulting after the doublet. To unravel the physical process resulted in this feature, we use space geodetic measurements to derive the surface displacements and stress field associated with the doublet. The derived stress field shows a staggering 29° rotation occurred in a horsetail splay fault structure where many normal-faulting earthquakes happened. The large stress rotation indicates the doublet released considerable stress and may result in a heterogeneous stress field due to the stress change. The combination of the identified horsetail structure and stress rotation can help better explain the occurrence of pervasive normal-faulting earthquakes.

1. Introduction

Earthquakes, manifested as sudden shear dislocation across the fault, play a pivotal role in releasing tectonic stresses accumulated within the Earth's crust at interseismic period. The dislocation process is often depicted by the double-couple force model (Kasahara, 1981). In accordance with this model, stress drop mostly occurs in the shear direction (shear stress) parallel with the fault interface, with no or little stress drop in the fault normal direction. Consequently, stress rotation, a change of the principal stress direction relative to that before the earthquake, accommodate the altered stress state (Michael, 1987). Precise stress rotation is critical to understand the absolute stress level and the future seismic hazard (X. Wang & Zhan, 2020).

Here we show a noteworthy instance of stress rotation, the 5 February 2023, Turkey-Syria Mw7.8 & 7.7 doublet. The Mw7.8 event first ruptured multiple fault segments along the East Anatolian Fault (EAF) system. Nine hours later, the Mw7.7 event took place to the northeast of the Mw7.8 epicenter, located within the Anatolian plate. The EAF is a left-lateral transform-type plate boundary, yet many normal-faulting aftershocks emerged in this region (see Figures 1b–1d). Normal-faulting events have increased from only 16% of earthquakes occurred in the last 4 decades before the doublet (as early as the first available mechanism in GCMT catalog) to 48% (Mw7.8) and

Writing – original draft: Zhangfeng Ma, Chenglong Li, Shengji Wei
Writing – review & editing: Zhangfeng Ma, Yu Jiang, Xinzhong Yin, Yosuke Aoki, Sang-Ho Yun, Shengji Wei

45% (Mw7.7) of the aftershock catalog (Figure 1d). In contrast, strike-slip events decreased from 76% of all focal mechanisms before the doublet to 34% (Mw7.8) and 37% (Mw7.7) of the aftershock catalog. Changes in earthquake types before and after earthquakes requires great stress change/rotation (Bohnhoff et al., 2006), due to the co-seismic slip on the faults (King et al., 1994).

Remarkably, the 2023 Mw7.8 & 7.7 doublet marked the first seismic occurrence of such magnitude in the area since 1114 (Figure 1a) (Carena et al., 2023; Gallovič et al., 2020; Pousse-Beltran et al., 2020). The northern part of the EAF, owing to the relative motion between the Anatolian and Arabian plates, stands recognized as a pivotal seismogenic zone capable of giving rise to formidable earthquakes (Güvercin et al., 2022; Turkelli et al., 2003). However, the ∼130-year silence of the southern part of the EAF broken by this Mw7.8 event has brought awareness again to the fact that faults characterized by distributed relatively low strain rate also harbor the potential to generate significant seismic events (K. Wang et al., 2021). The active tectonic in this region are predominantly characterized by strike-slip motion, but the intricate interplay of factors such as crustal thickening, rotational effects, variations of the EAF geometry (Vanacore et al., 2013), and the intricate interaction of strain between primary and secondary faults collectively pose a challenge in deciphering the underlying structural configurations of background stress in the presence of low strain rates (Cakir et al., 2023; Reilinger et al., 2006; Weiss et al., 2020; Zhao et al., 2021).

Here we use space geodetic observations to constrain the fault geometry, slip distribution and stress field associated with the doublet, to shed some new lights on the stress change/rotation and their relationship with dramatic seismicity focal mechanism variation. We first derive complete high resolution 3-dimensional (3D) surface displacements using abundant space geodetic data and multiple state-of-the-art data processing techniques, then we invert for detailed fault geometry and slip distribution directly using 3D displacement field. This is followed by stress analysis caused by the co-seismic slip of the doublet. Finally, we propose a fault model and stress field that accommodates both co-seismic slip and the focal mechanism changes to the normal faulting dominating aftershocks.

2. Observations and Methods

2.1. Space Geodetic Data and Processing

The doublet was extremely well recorded by the Sentinel-1/2 and ALOS-2 satellites, with multiple images acquired before and after the doublet. To process these data, we applied five different techniques in the data processing, including Interferometric Synthetic Aperture Radar (InSAR), Range Split Spectrum Interferometry (RSSI), Multiple Aperture Interferometry (MAI), Burst Overlap Interferometry (BOI) and Pixel Offset Tracking (POT). InSAR and RSSI are to capture the displacements in the range direction, which is sensitive to the motion in the East-West (EW) and vertical directions. We applied these two techniques in Sentinel-1 Terrain Observation with Progressive Scan (TOPS) data and ALOS-2 data (Stripmap and ScanSAR mode). BOI and MAI are to obtain the displacement maps in the radar azimuth direction, which is sensitive to the North-South (NS) motion. BOI can be only applied in the TOPS data due to its requirement of high doppler centroid frequency difference between consecutive radar bursts (De Zan & Guarnieri, 2006). We only performed MAI on the ScanSAR data by the advantage of its large azimuth Doppler frequency difference between consecutive bursts. POT data can obtain the displacements both in range and azimuth direction. We applied it in TOPS, Stripmap and Sentinel-2 optical data. Note that POT for Sentinel-2 data directly derives the NS and EW displacements instead of the range and azimuth direction for radar data. See Texts S1.1–S1.5 and Tables S1 and S2 in Supporting Information S1 for the detailed data and method description. We obtained a total of 36 displacement maps (Figure S1 in Supporting Information S1). With these data sensitive to different directions, we can further derive 3D co-seismic surface displacements.

2.2. The Derivation of 3D Displacement Fields

An important goal of getting geodetic observations for earthquakes is to use them for slip model inversions. However, with 36 displacement images, as derived in Section 2.1, the amount of data used in the inversion is enormous, even though each image is down-sampled to a few thousands of data points, which is usually necessary to preserve the resolution on sufficient details. In addition, it is also very difficult to properly assign weighting factors between various displacement images in the inversion. To reduce the size of the data set in the inversion

10.1029/2023GL107788

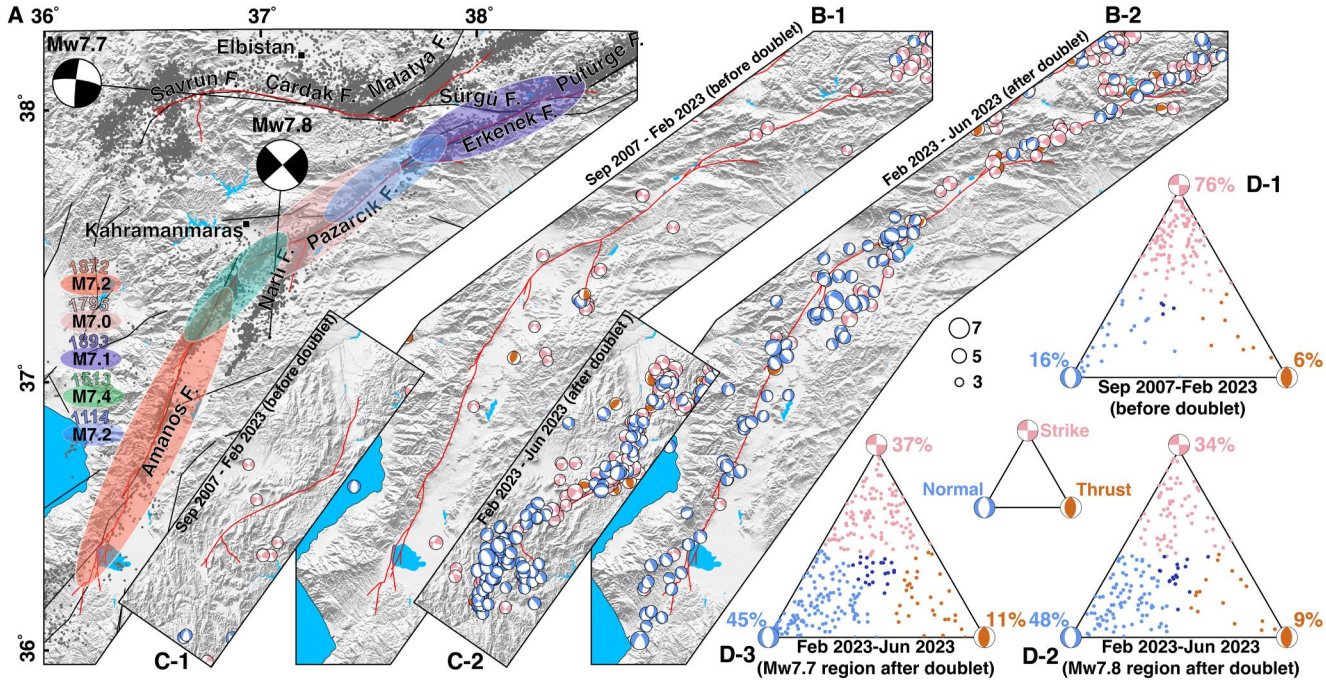

Figure 1. The background of the study area. (a) Aftershocks, simplified fault trace, and historical earthquakes. (b-1, b-2) Focal mechanisms related to the main shock before and after the earthquake doublet. (c-1, c-2) Focal mechanisms related to the second shock. (d-1) The classified earthquakes for (b-1) and (c-1). (d-2) The classified earthquakes for (b-2). (d-3) The classified earthquakes for (c-2). Aftershocks are in gray dots. Fault traces are in red lines. Focal mechanisms are from https://deprem.afad.gov.tr/event-focal-mechanism.

and avoid weighting selection, as well as to have a more intuitive visualization of the deformation, it is pivotal to calculate robust and comprehensive 3D displacement fields for the doublet.

To this end, we employed the Strain Model and Variance Component Estimation (SM-VCE) toolbox (J. Liu et al., 2022) based on the 36 observations. The SM-VCE method incorporates strain model to account for the spatial correlation of adjacent points' displacements as well as the employment of VCE algorithm to weight multiple observations. During the derivation, prior weight is not required since the VCE can automatically weight different observations through iterations. The only input parameter is the square sliding window size. Here, we use 15 pixels (~150 m) as in previous studies (J. Liu et al., 2019; Wei et al., 2022), which is determined based on the tradeoff between the accuracy and the computational burden. During calculation, we exclude the inhomogeneous points to the other side of the fault (Hu et al., 2021), to ensure that the opposite displacements on both sides of the fault will not affect each other in the derivation.

2.3. Fault Geometry and Geodetic Slip Inversion

Based on the clear capture of sharp near-fault displacement contrast, it is straightforward to determine the strike of each fault segment. Consequently, we use 28 fault segments to approximate the along strike fault geometry variation of the doublet. We adopt a resolution-based mesh algorithm to reduce the displacement into sparse points (Lohman & Barnhart, 2010; Lohman & Simons, 2005). The location of data samples was determined through an initial geodetic inversion, where all fault segments were assumed to be vertical. The resolution cells obtained from this process were populated with mean values from the original 3D displacements. To ensure an accurate representation of slip distribution near the Earth's surface, we increased the density of offsets data around the fault traces, which is particularly critical to resolve the shallowest part of the rupture. Specifically, we sampled the near-field offset data starting from the minimum resolution of ~250 m (see Figure S5 in Supporting Information S1), considering a patch size of 1 km by 1 km at the shallowest depth (Jin & Fialko, 2020).

To constrain more detailed fault geometry, that is, the dipping angle (include dip direction) of each fault segment, we adopted a tailored Markov Chain Monte Carlo approach to invert the resampled data. We targeted the dipping angle of 28 segments and utilized 128 parallel chains to capture their probability distribution. Post 10,000

iterations, all dipping angles stabilized, yielding the resulting fault geometry. Rectangular segments approximating fault geometry were then set to 30 km depth. Each segment was subdivided into smaller slip patches, with the along strike size increase from 1 km gradually in the down-dip direction. This growth followed a geometric progression with a 1.3 incremental ratio, ensuring consistent model resolution with increasing depth (X. Xu et al., 2016).

Subsequently, strike-slip and dip-slip Green's functions were computed for each resampled point (Okada, 1985). We set the relative weight of the displacements between each direction to the same values. The weight for each direction is the standard deviation values of all sampled points in each triangle. While the strike slip component adhered to a positivity constraint (e.g., no opposite slip direction), no restrictions were placed on the dip slip component. Nevertheless, dip slip smoothing was enhanced to twice of that for strike slip to mitigate spatially oscillating slip patterns (Jin & Fialko, 2020). Furthermore, distance-based constraints were introduced for neighboring patches and intersecting segments (X. Xu et al., 2016). The bottom layer of fault segments is constrained by a soft zero slip boundary conditions, while the patches nearly surface remained unconstrained. Ultimately, constrained linear square was employed to solve the slip distribution, facilitating accurate determination of slip distribution.

2.4. The Derivation of Local Stress Field Through Near Field Displacements

With the 3D displacement fields, we employed a 3D deviatoric stress tensor inversion technique to derive the associated stress field. This method operates under the assumption that slip is parallel to the shear stress, as in accordance with the Wallace-Bott hypothesis (Michael, 1984). Through it, we were able to ascertain the orientation of the stress tensor across three dimensions. Notably, similar methodologies have applied in the analysis of the 2010 Mw7.1 El-Mayor Cucapah and the 2019 Ridgecrest earthquake sequences, where field surface observations were employed as well (Fletcher et al., 2016; Milliner et al., 2022).

We leveraged 3D displacement maps and calculated the near fault (<500 m) rupture at a regular along strike interval of 100 m (Figure S15 in Supporting Information S1). To incorporate the spatial heterogeneities of stress along the rupture, we partitioned the rupture into discrete segments corresponding to individual seismic events (Figure S16 in Supporting Information S1), and subsequently delineated their respective trajectories. Within each segment, at least 30 slip vectors are required to ensure a diverse spectrum of fault orientations that is pivotal for a robust determination of the stress tensor. Our stress inversion procedure hinged upon the L1 norm minimization, as inherited from Milliner et al. (2022), which exhibits reduced sensitivity to anomalies relative to the conventional L2 norm. To prevent overfitting and enhance stress coherence along the rupture, an empirical damping constraint was added during the inversion. This penalized stress orientation shifts between nearby sections, enhancing overall stress consistency. To assess stress model uncertainties, we used bootstrapping, which involved iteratively replacing slip vectors and recalculating the stress tensor, yielding variations for uncertainty estimates and model evaluation.

3. Results and Discussions

3.1. 3D Co-Seismic Displacements

Figures 2a–2c presents 3D displacements, in an intuitive North, East, Up convention, same to global navigation satellite system (GNSS) displacements. Results reveal a small root-mean-square error (Figure S2 in Supporting Information S1), under 10 cm overall across three directions, correlating highly at a coefficient of 0.95 with GNSS displacements (Figure S3 in Supporting Information S1). The described horizontal shift showcases Arabian Plate rotation northward and Anatolian Plate westward trend (Altamimi et al., 2017). An important feature of the derived 3D displacement fields is nearly continuous data points across the faults, which is rarely available for the historical events, except recent ones (e.g., Maduo and Ridgecrest). In these 3D displacements, we capture clearly multiple fault ruptures particularly in the dominating EW displacement, marking major surface ruptures along Amanos, Pazarcık, Erkenek, Çardak, and Savrun Faults (Figures 2a and 2b). The surface rupture traces we derived align well with field surveys (Reitman et al., 2023). Co-seismic horizontal displacement of the doublet mainly features left-lateral strike-slip motion, with at least six major fault bends/branches (Figure 2). Sizable slips were identified along Pazarcık (Mw7.8) and Çardak (Mw7.7) Faults. Asymmetric horizontal motion across faults (arrow contrast near fault in Figure 2a), and more heterogenous vertical deformation highlights both complex fault geometry and slip distribution.

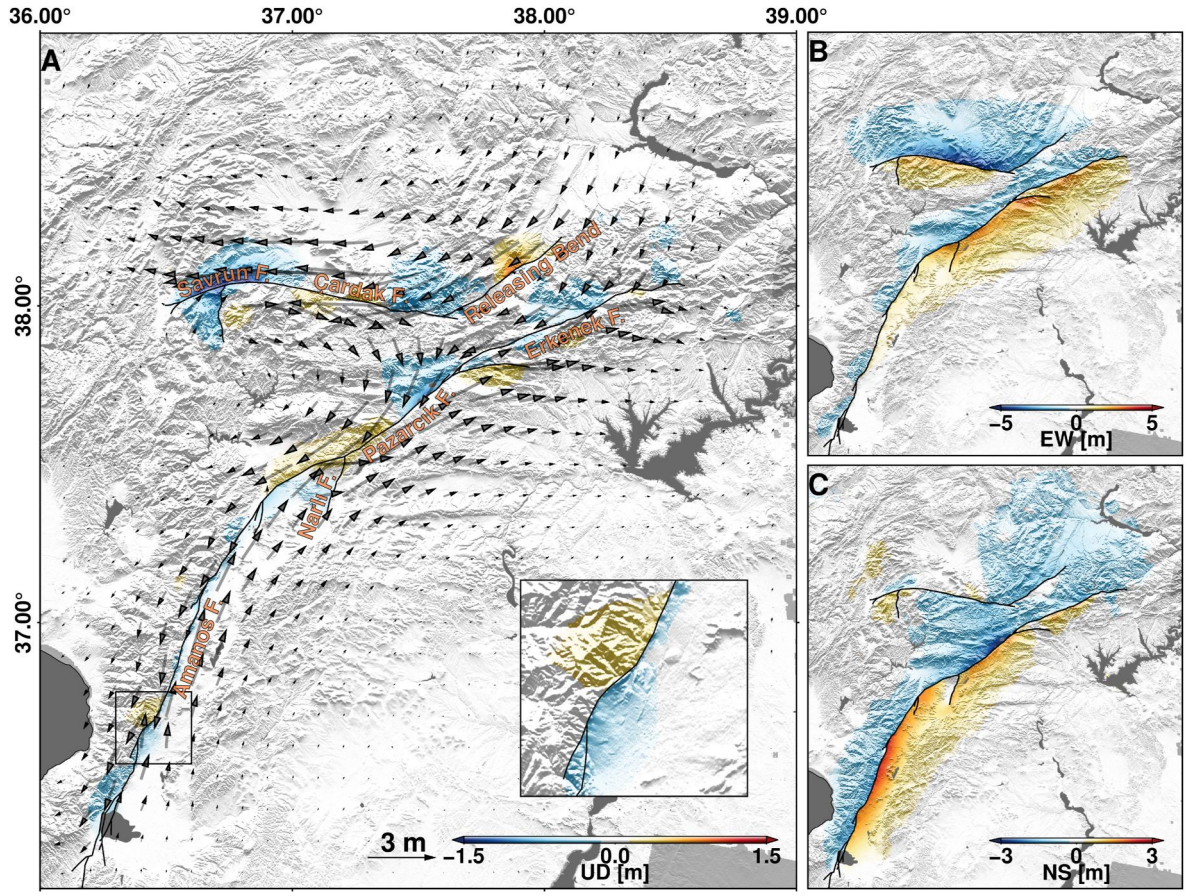

Figure 2. 3D displacements. (a) Vertical displacement. Arrows represent the horizontal displacements. The rectangle area inset represents the fault kink. (b, c) East-West (EW) and North-South (NS) displacements. The black solid lines are the simple fault trace.

For instance, at the Amanos segment's kink (Figure 2a zoom-in), vertical motion clearly shifts from subsidence at the west of the fault to uplift at the east, suggesting strong compression (extension) at the concave (convex) side of the kink. Similar geometry induced compression (extension) can also be observed for other kinks of the Mw7.8 event. However, the vertical deformation pattern outlines stronger subsidence near the Savrun Fault (the releasing bend of Çardak Fault) and its branches can't be explained in the same way. This pronounced subsidence requires larger normal slip component on the Savrun Fault system (Mw7.7) than the Mw7.8 event. This larger normal slip indicates a higher level of extensional stress within the Anatolian plate, likely associated with the distributed deformation propagating from the releasing bend on EAF. This contrast between the strength of normal-faulting component between the doublet also suggests regional stress complexity near the Çardak Fault's terminus, possibly forming these extensional horsetail splay structures. Besides kinks and branches, relatively smooth fault strike variation along with more heterogeneous variation of subsidence or uplift due to dipping angle and rake direction changes, providing key constraints for detailed fault geometry and slip distribution in the inversion.

3.2. Fault Geometry and Slip Distribution

Figures S6–S7 in Supporting Information S1 and Figures 3a and 3b present the inverted fault geometry and slip distribution. The inferred fault geometry shows that most of the fault segments along the EAF exhibit westward dipping. The Çardak and Savrun Faults exhibit northward dipping and have relatively shallow dipping angles along with its branch, which is highly consistent with the well-constrained locations of aftershocks (Figure 3a) (Ding et al., 2023). The Çardak and Savrun Faults oriented nearly perpendicular to the plate motion direction of the Anatolian Plate motion and therefore may have experienced significant horizontal strain. A combination of slip acting on the fault plane and distributed deformation off fault due to this long-lived horizontal strain can cause such shallow dipping angles (Johnson, 2018). In comparison, variations in the dipping angle of the mainshock

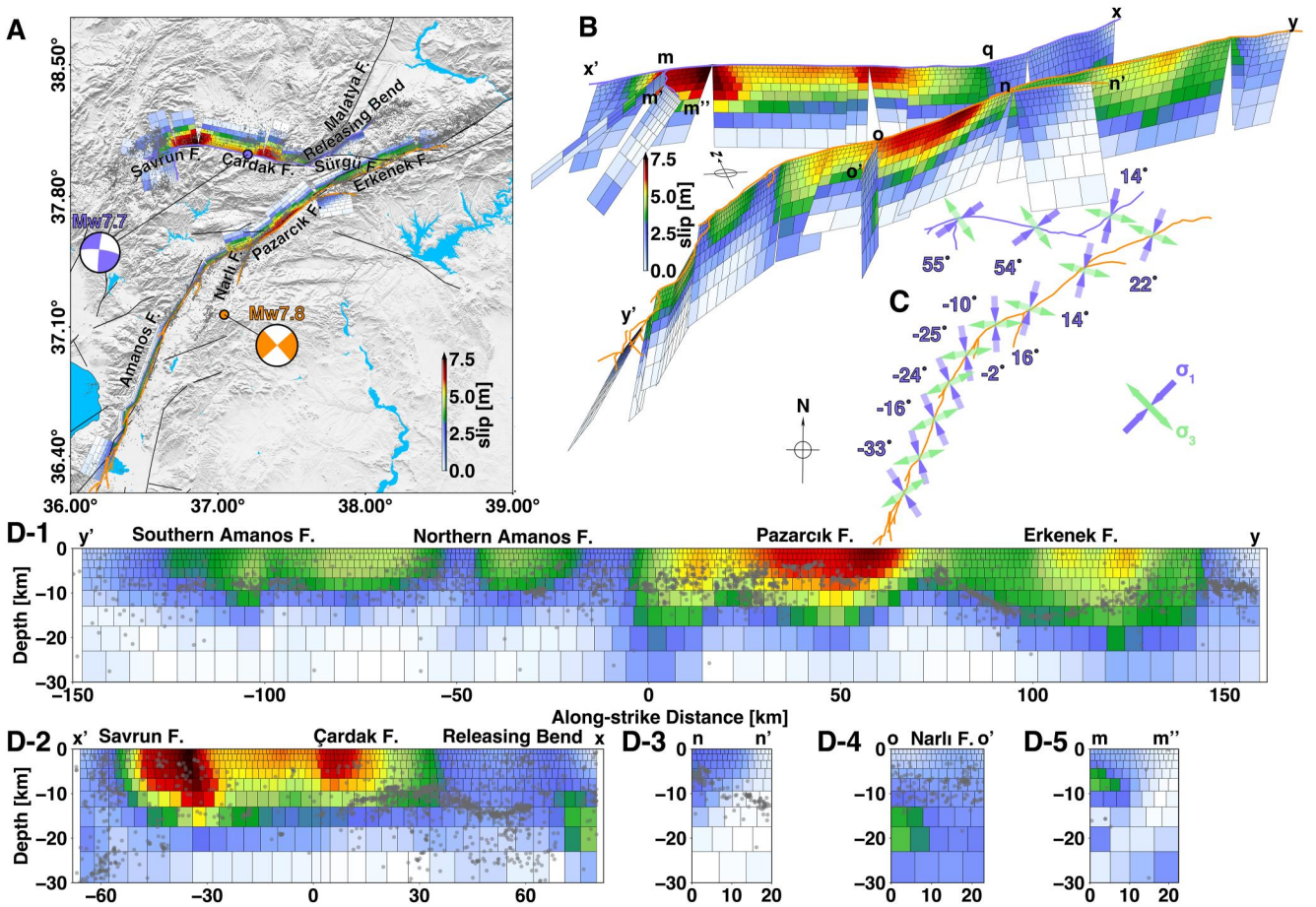

Figure 3. Slip distribution, relative horizontal displacements, and stress fields. (a) 2D slip distribution and seismicity. (b) Derived fault geometry and 3D slip distribution. (c) Stress field. (d-1–d-5) Faults slip along the strike direction.

fault may be related to changes in fault strike relative to the movement direction of the Arabian Plate. Along the Amanos Fault, where the fault strike is more parallel to the large-scale plate motion, the fault is near vertical, while the Pazarcik and Erkenek Faults show stronger northwest dipping geometry where their strikes rotate ~25° clockwise relative to Amanos Fault.

The slip model effectively accounts for 3D displacements (Figure S10 in Supporting Information S1), reducing variance by ~95%. Average residual displacements in EW, NS, and UD directions are 7.2, 6.3, and 4.1 cm, respectively. Slip distribution exhibits multiple major asperities along total fault length of ~500 km, similar to previous models (Barbot et al., 2023; Okuwaki et al., 2023). The Mw7.8 event's slip pattern comprises at least six asperities, with the most prominent one on the Pazarcık segment, aligned with the reported supershear segment (Melgar et al., 2023; Okuwaki et al., 2023). The Erkenek segment to the north displays deeper (~20 vs. 10 km) slip than the Amanos segment to the south, suggesting variation of locking depth along the EAF. However, northward slip halted abruptly at a restraining bend with a sharp dipping change, highlighting potential geometrical rupture arrest. For Mw7.7 event, two major asperities emerge: one on the Savrun segment (matching supershear segment (Jia et al., 2023; C. Liu et al., 2023; L. Xu et al., 2023)) and another on the Çardak segment. On the releasing bend to the northeast of the epicenter, the slip amplitude is much lower, possibly due to significant strike change, inducing stress field that does not support large rupture. This could also be understood as that this fault segment is more parallel with the EAF, where substantial slip already took place in the Mw7.8 event (Erkenek segment).

Checkerboard tests and pseudo-resolution matrix spatial structure (Text S2 and Figures S8 and S9 in Supporting Information S1) demonstrate robust and detailed inversion resolution, affirming slip asperity reliability. Complementary spatial feature could be observed between slip and aftershock distribution (Figure 3d), particularly on

the Erkenek segment. The southern sections of the Mw7.8 event exhibit a shallower seismogenic zone, possibly linked to a more heterogeneous stress distribution that may not be uniformly released as observed in the northern regions. Therefore, we observe weaker complementary distribution between slip and aftershocks. Notably, our slip model does not show shallow slip deficit (Figure S11 in Supporting Information S1), not like in the preliminary report (Barbot et al., 2023). This is likely because we used much more robust near fault data in the slip inversion. Enhanced near-field observations, including Stripmap, ScanSAR MAI, and optical POT results, allow us to resolve these key observations much better (Figures S12 and S14 in Supporting Information S1). The lack of near-field observations and the regularization of shallow patch interactions in the inversion may give rise to a false impression of shallow slip deficit (Jiang et al., 2013). The slip of larger shallow patches corresponds to displacements further away from the fault, so larger shallow patch size can suppress this false impression even without very near-field constraints (Figures S13 and S14 in Supporting Information S1). However, to obtain a finer slip distribution of shallow patches, near-field observations are necessary.

3.3. Stress Fields and the Extensional Horsetail Splay Fault Structure

Figure 3c illustrates stress field directions computed from near-field co-seismic displacements (Figure S15 in Supporting Information S1). The results illustrate that EAF's maximum principal stress (σ_1) direction derived from stress inversion (Figures S17 and S18 in Supporting Information S1) shifted from −33° to 22° (clockwise from north), mirroring latitudinal transition in plate motion. σ_1 direction along the rupture of the Mw7.7 changed from 14° eastwards to 55° westwards, reflecting substantial stress variation within the Anatolian Plate as the distance increase away from the EAF. σ_1 direction of 14° at releasing bend aligns with that near the Erkenek fault, suggesting the stress field here is dominated by the plate boundary, this is consistent with earlier interpretation of the slip amplitude on these fault segments. Stress inversion was also conducted on the aftershock focal mechanisms to deduce principal stress directions, revealing background stress after the mainshocks (Figure S19 in Supporting Information S1). Due to aftershock productivity and focal mechanism availability, less certain results emerged in sparsely distributed focal mechanism regions. As a result, we only obtain stable principal stress directions in three areas (m, p, n in Figure 4a). Remarkably, these areas align with the three regions displaying the large coseismic slip. Therefore, we can compare the stress fields associated with the coseismic rupture and aftershocks to reveal the stress change/rotation due to the mainshocks in these three regions.

Assuming co-seismic background stress direction aligns with local tectonic stress (Milliner et al., 2022), Savrun Fault's stress rotation angle is calculated as −29° (Figure 4a, p region). Following a relation derived from a 2D stress analysis (Hardebeck & Hauksson, 2001), stress drop ratio depends on the rotation angle of σ_1 and the angle between σ_1 and fault strike (inset plot in Figure 4a). The values we derive for region p suggests ∼89% release of deviatoric stress. In comparison, region n stress rotation angle is just −2°, but it also released around 65% of the deviatoric stress, due to near 45° angle between σ_1 and fault strike. In this case stress rotation angle is much more sensitive to stress drop ratio. In region m, −18° stress rotation indicates approximately 72% deviatoric stress release. The level of stress rotation is actually much larger than that reported in the 2019 Ridgecrest earthquakes (X. Wang & Zhan, 2020), as the slip amplitude of Turkey doublet is larger. Using the derived stress drop ratios and stress drop, the absolute pre-stress amplitude could be further derived. Based on coseismic slip models, the average coseismic stress drop in three box regions (m, n and p in Figure 4a), are calculated as 7.2, 7.0, and 8.6 MPa, respectively, and therefore the corresponding pre-stresses are 10, 10.8, and 9.7 MPa. Indeed, pre-stresses estimated in this way are much lower than the lithostatic stress at a few km depth, suggesting either weak fault zones and/or high pore fluid pressure.

The geometry and slip direction (rake) of faults in region p (Figure 4a), where maximum stress rotation took place, offer further insights into large number of normal-faulting aftershocks. Note that here the fault traces are color-coded by their average rake angle. The Savrun Fault, shaped as a horsetail, transitions from strike-slip to slight normal-faulting westwards, and to almost pure normal-faulting on the branching fault. We attribute this geometry and rake changes to the extensional horsetail splay faults (Kim & Sanderson, 2006), which are branches produced at the tip of a strike-slip fault, typically manifesting as either normal faults or thrust faults, depending on the stress concentration characteristics at the fault branch. Stress concentration at fault tips leads to damage zones, which could be classified into three areas (Figure 4b) (Scholz et al., 1993): the shearing structure ahead of the rupture front, the compressional quadrant to the right side of a left-lateral fault (or the left side for a right-lateral fault), and the dilatational quadrant to the left side of the fault (or the right side for a right-lateral fault). Within the dilatational quadrant, extensional horsetail splay faults are commonly observed (Kim et al., 2004). They branch

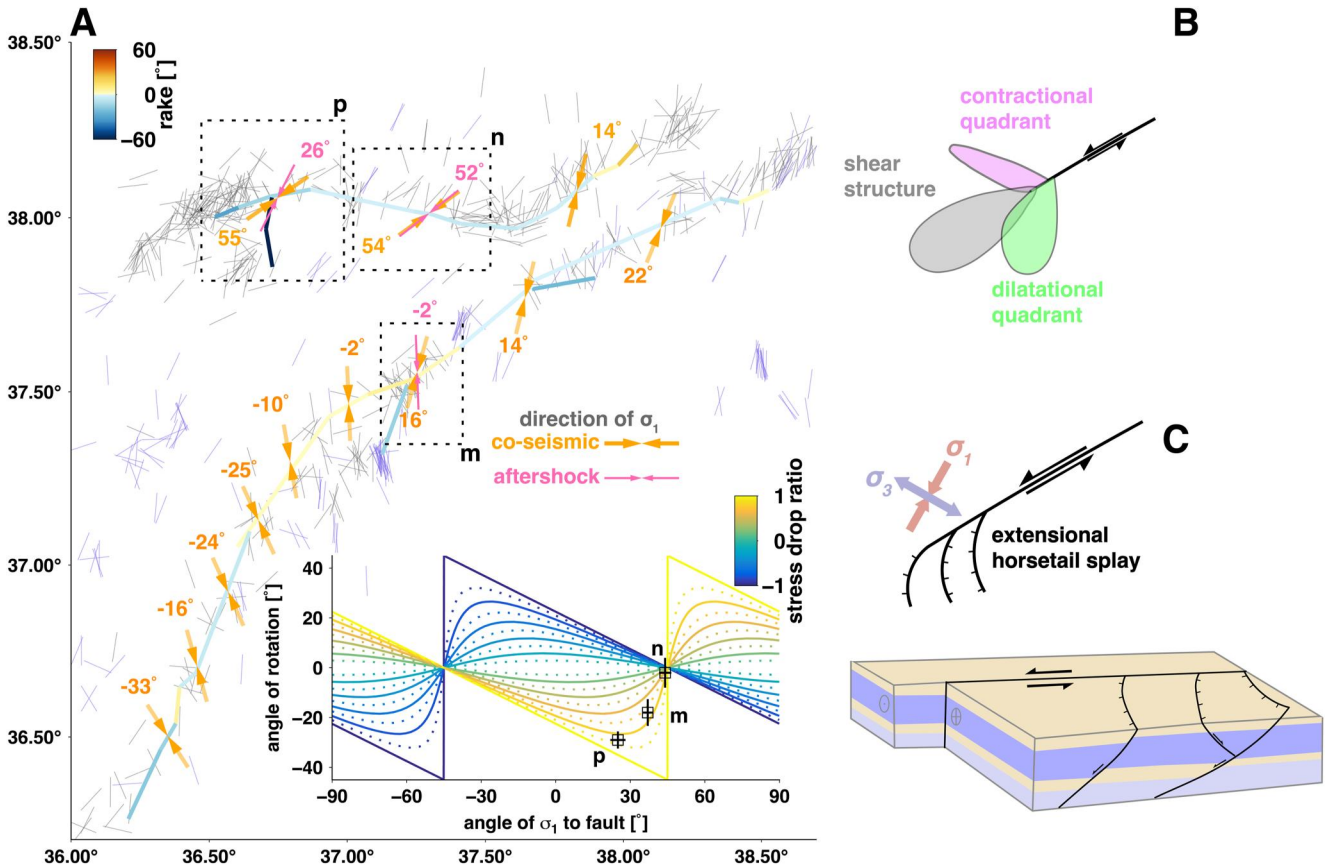

Figure 4. (a) σ_1 directions and stress drop ratios. Short purple and gray lines in the main plot mean the P axes of focal mechanisms before and after the doublet, respectively. Orange and pink arrows are results from 3D co-seismic displacements and aftershock focal mechanisms, respectively. (b) The conceptional model for three components of a left-lateral fault, modified from Scholz et al. (1993). (c) The conceptional model for the extensional horsetail splays and their 3D shape.

from the main fault, bending towards the σ_1 direction, often adopting a wedge shape (Kim & Sanderson, 2006). With fault strikes more parallelly to the σ_1 (P-axis) direction, T-axis orients nearly perpendicular to fault strike (e.g., region p). This background stress often generates normal-faulting earthquakes (Bohnhoff et al., 2006), matches with observations in region p. The extensional stress field could also be inferred from the 3D displacement (Figure 2a) where the horizontal displacement showed larger eastward motion to the eastern side of the branching fault than that to the western side. A conceptual model is presented in Figure 4c to illustrate the interpreted extensional horsetail splay faults in a 3D view.

The characteristics of strike-slip and normal-faulting behavior of both the mainshocks and aftershocks may represent a regular way of leasing long-term accumulated stress. However, there are some differences between the doublet. For the Mw7.8 event, the mainshock rupture shows pure strike-slip on near vertical faults, but its aftershocks are dominated by normal faulting events, likely related to the releasing bends of the EAF. In contrast, the Mw7.7 mainshock rupture shows substantial normal component with shallower dipping angles, followed by larger number of normal faulting aftershocks in a horsetail splay fault system. But since the slip rates of the faults inside the Anatolian plate (e.g., Mw7.7 event) are low, this area does not show much background seismicity, the normal faulting events there mostly occurred after big strike-slip earthquakes as aftershocks.

4. Conclusions

In this study, we address a question of why normal-faulting aftershocks are frequently observed in the strike-slip fault system of the February 2023 Turkey-Syria earthquake doublet. Using a wide range of space geodetic data, we have performed a comprehensive analysis on the 3D displacements, slip inversion and stress analysis. Our results show that the three regions with rich aftershocks and large coseismic slip release considerable deviatoric

stress. The maximum stress rotation angle among the Savrun Fault even reached a staggering 29°. From the slip model of the Savrun Fault and its branch fault identified as extensional horsetail splay fault structure, we have captured their obvious normal-faulting characteristics. It indicates that the Savrun Fault and its branch fault are inherently capable of producing normal-faulting earthquakes, whereas the co-seismic stress rotation may enhance the normal-faulting characteristics there. This may be a microcosm of the whole region. Due to fault geometry and stress concentration, the strike-slip fault system may have the ability to generate normal-faulting earthquakes, and co-seismic stress rotation may aggravate their occurrence.

Data Availability Statement

Focal mechanisms data can be freely downloaded from https://deprem.afad.gov.tr/event-focal-mechanism. The simple fault trace and ruptured trace can be obtained from Reitman et al. (2023). Most of figures were drawn by Generic Mapping Tools 6.4.0 software (https://www.generic-mapping-tools.org/download/; Wessel et al., 2019). SMVCE software can be download from https://gip.csu.edu.cn/radar/gongkaicontent.jsp?urltype=news.NewsContentUrl&wbtreeid=1137&wbnewsid=3072, and the unzip code will be sent to the email address filled. CtSent toolbox for Sentinel-1 interferometric processing used in this paper can be downloaded from Zenodo (Ma, 2021). Codes for unwrapping operation can be downloaded from Zenodo (Ma, 2024). Our 3D displacement maps and slip distribution can be downloaded from Zenodo (Ma et al., 2023).

Acknowledgments

The authors thank the editor Lucy Flesch, Prof. Xiaohua Xu in University of Science and Technology of China and Prof. Wenbin Xu in Central South University for their insightful comments which help us greatly improve the manuscript. This research was supported by Singapore MOE project (MOE-MOET32021-0002) and the Earth Observatory of Singapore via its funding from the National Research Foundation Singapore and the Singapore Ministry of Education under the Research Centers of Excellence initiative. This work comprises EOS contribution number 572. We thank Dr. Jihong Liu and Dr. Xing Li in King Abdullah University of Science and Technology for their guidance in 3D displacement inversion. We thank Dr. Christopher Milliner in NASA Jet Propulsion Laboratory for his patient answers and fruitful discussions on the stress inversion. We thank Dr. Xin Wang in Institute of Geology and Geophysics, Chinese Academy of Sciences for his fruitful discussions on the splay faults. We thank Dr. Haipeng Luo and Dr. Hongyu Zeng in Earth Observatory of Singapore for their insightful suggestions on the stress rotation. We acknowledge the Turkey Disaster and Emergency Management Authority (AFAD) for providing focal mechanisms. We acknowledge Nevada Geodetic Laboratory for providing GNSS displacement data. We also thank USGS for providing fault trace. We acknowledge Japan Aerospace Exploration Agency for providing ALOS-2 data under the Grant ER3A2N139. We acknowledge European Space Agency for freely providing Sentinel-1/2 data.

References

Altamimi, Z., Métivier, L., Rebischung, P., Rouby, H., & Collilieux, X. (2017). ITRF2014 plate motion model. *Geophysical Journal International*, *209*(3), 1906–1912. https://doi.org/10.1093/gji/ggx136

Barbot, S., Luo, H., Wang, T., Hamiel, Y., Piatibratova, O., Javed, M. T., et al. (2023). Slip distribution of the February 6, 2023 Mw 7.8 and Mw 7.6, Kahramanmaraş, Turkey earthquake sequence in the East Anatolian Fault Zone. *Seismica*, *2*(3). https://doi.org/10.26443/seismica.v2i3.502

Bohnhoff, M., Grosser, H., & Dresen, G. (2006). Strain partitioning and stress rotation at the North Anatolian fault zone from aftershock focal mechanisms of the 1999 Izmit Mw= 7.4 earthquake. *Geophysical Journal International*, *166*(1), 373–385. https://doi.org/10.1111/j.1365-246X.2006.03027.x

Cakir, Z., Doğan, U., Akoğlu, A. M., Ergintav, S., Özarpacı, S., Özdemir, A., et al. (2023). Arrest of the Mw 6.8 January 24, 2020 Elaziğ (Turkey) earthquake by shallow fault creep. *Earth and Planetary Science Letters*, *608*, 118085. https://doi.org/10.1016/j.epsl.2023.118085

Carena, S., Friedrich, A. M., Verdecchia, A., Kahle, B., Rieger, S., & Kübler, S. (2023). Identification of source faults of large earthquakes in the Turkey-Syria Border Region between 1000 CE and the present, and their relevance for the 2023 Mw 7.8 Pazarcık earthquake. *Tectonics*, *42*(12), e2023TC007890. https://doi.org/10.1029/2023TC007890

De Zan, F., & Guarnieri, A. M. (2006). TOPSAR: Terrain observation by progressive scans. *IEEE Transactions on Geoscience and Remote Sensing*, *44*(9), 2352–2360. https://doi.org/10.1109/tgrs.2006.873853

Ding, H., Zhou, Y., Ge, Z., Taymaz, T., Ghosh, A., Xu, H., et al. (2023). High-resolution seismicity imaging and early aftershock migration of the 2023 Kahramanmaraş (SE Türkiye) Mw7.9 & 7.8 earthquake doublet. *Earthquake Science*, *36*(6), 417–432. https://doi.org/10.1016/j.eqs.2023.06.002

Fletcher, J. M., Oskin, M. E., & Teran, O. J. (2016). The role of a keystone fault in triggering the complex El Mayor–Cucapah earthquake rupture. *Nature Geoscience*, *9*(4), 303–307. https://doi.org/10.1038/ngeo2660

Gallovič, F., Zahradník, J., Plicka, V., Sokos, E., Evangelidis, C., Fountoulakis, I., & Turhan, F. (2020). Complex rupture dynamics on an immature fault during the 2020 Mw 6.8 Elazığ earthquake, Turkey. *Communications Earth & Environment*, *1*(1), 40. https://doi.org/10.1038/s43247-020-00038-x

Güvercin, S. E., Karabulut, H., Konca, A. Ö., Doğan, U., & Ergintav, S. (2022). Active seismotectonics of the East Anatolian Fault. *Geophysical Journal International*, *230*(1), 50–69. https://doi.org/10.1093/gji/ggac045

Hardebeck, J. L., & Hauksson, E. (2001). Crustal stress field in southern California and its implications for fault mechanics. *Journal of Geophysical Research*, *106*(B10), 21859–21882. https://doi.org/10.1029/2001JB000292

Hu, J., Liu, J., Li, Z., Zhu, J., Wu, L., Sun, Q., & Wu, W. (2021). Estimating three-dimensional coseismic deformations with the SM-VCE method based on heterogeneous SAR observations: Selection of homogeneous points and analysis of observation combinations. *Remote Sensing of Environment*, *255*, 112298. https://doi.org/10.1016/j.rse.2021.112298

Jia, Z., Jin, Z., Marchandon, M., Ulrich, T., Gabriel, A. A., Fan, W., et al. (2023). The complex dynamics of the 2023 Kahramanmaraş, Turkey, Mw 7.8-7.7 earthquake doublet. *Science*, *0*(0), eadi0685. https://doi.org/10.1126/science.adi0685

Jiang, G., Xu, C., Wen, Y., Liu, Y., Yin, Z., & Wang, J. (2013). Inversion for coseismic slip distribution of the 2010 Mw 6.9 Yushu Earthquake from InSAR data using angular dislocations. *Geophysical Journal International*, *194*(2), 1011–1022. https://doi.org/10.1093/gji/ggt141

Jin, Z., & Fialko, Y. (2020). Finite slip models of the 2019 Ridgecrest earthquake sequence constrained by space geodetic data and aftershock locations. *Bulletin of the Seismological Society of America*, *110*(4), 1660–1679. https://doi.org/10.1785/0120200060

Johnson, K. M. (2018). Growth of fault-cored anticlines by flexural slip folding: Analysis by boundary element modeling. *Journal of Geophysical Research: Solid Earth*, *123*(3), 2426–2447. https://doi.org/10.1002/2017JB014867

Kasahara, K. (1981). Earthquake mechanics. Mecanique des Seismes.

Kim, Y.-S., Peacock, D. C. P., & Sanderson, D. J. (2004). Fault damage zones. *Journal of Structural Geology*, *26*(3), 503–517. https://doi.org/10.1016/j.jsg.2003.08.002

Kim, Y.-S., & Sanderson, D. J. (2006). Structural similarity and variety at the tips in a wide range of strike–slip faults: A review. *Terra Nova*, *18*(5), 330–344. https://doi.org/10.1111/j.1365-3121.2006.00697.x

King, G. C. P., Stein, R. S., & Lin, J. (1994). Static stress changes and the triggering of earthquakes. *Bulletin of the Seismological Society of America*, *84*(3), 935–953. https://doi.org/10.1785/BSSA0840030935

Liu, C., Lay, T., Wang, R., Taymaz, T., Xie, Z., Xiong, X., et al. (2023). Complex multi-fault rupture and triggering during the 2023 earthquake doublet in southeastern Türkiye. *Nature Communications*, *14*(1), 5564. https://doi.org/10.1038/s41467-023-41404-5

Liu, J., Hu, J., Li, Z., Ma, Z., Shi, J., Xu, W., & Sun, Q. (2022). Three-dimensional surface displacements of the 8 January 2022 Mw6.7 Menyuan earthquake, China from Sentinel-1 and ALOS-2 SAR observations. *Remote Sensing*, *14*(6), 1404. https://doi.org/10.3390/rs14061404

Liu, J., Hu, J., Xu, W., Li, Z., Zhu, J., Ding, X., & Zhang, L. (2019). Complete three-dimensional coseismic deformation field of the 2016 Central Tottori earthquake by integrating left- and right-looking InSAR observations with the improved SM-VCE method. *Journal of Geophysical Research: Solid Earth*, *124*(11), 12099–12115. https://doi.org/10.1029/2018JB017159

Lohman, R. B., & Barnhart, W. D. (2010). Evaluation of earthquake triggering during the 2005–2008 earthquake sequence on Qeshm Island, Iran. *Journal of Geophysical Research*, *115*(B12). https://doi.org/10.1029/2010JB007710

Lohman, R. B., & Simons, M. (2005). Some thoughts on the use of InSAR data to constrain models of surface deformation: Noise structure and data downsampling. *Geochemistry, Geophysics, Geosystems*, *6*(1). https://doi.org/10.1029/2004GC000841

Ma, Z. (2021). Co-registration toolbox for Sentinel-1 [Software]. Zenodo. https://doi.org/10.5281/zenodo.4774694

Ma, Z. (2024). maerabubu/GT-CS-PU: Version1.0 [Software]. Zenodo. https://doi.org/10.5281/zenodo.10530903

Ma, Z., Li, C., Jiang, Y., Chen, Y., Yin, X., Aoki, Y., et al. (2023). 3D displacements for February 2023 Turkey-Syria earthquake doublet [Dataset]. Zenodo. https://doi.org/10.5281/zenodo.8405014

Melgar, D., Taymaz, T., Ganas, A., Crowell, B., Öcalan, T., Kahraman, M., et al. (2023). Sub- and super-shear ruptures during the 2023 Mw 7.8 and Mw 7.6 earthquake doublet in SE Türkiye. *Seismica*, *2*(3). https://doi.org/10.26443/seismica.v2i3.387

Michael, A. J. (1984). Determination of stress from slip data: Faults and folds. *Journal of Geophysical Research*, *89*(B13), 11517–11526. https://doi.org/10.1029/JB089iB13p11517

Michael, A. J. (1987). Stress rotation during the Coalinga aftershock sequence. *Journal of Geophysical Research*, *92*(B8), 7963–7979. https://doi.org/10.1029/JB092iB08p07963

Milliner, C. W. D., Aati, S., & Avouac, J. P. (2022). Fault friction derived from fault bend influence on coseismic slip during the 2019 Ridgecrest Mw 7.1 mainshock. *Journal of Geophysical Research: Solid Earth*, *127*(11), e2022JB024519. https://doi.org/10.1029/2022JB024519

Okada, Y. (1985). Surface deformation due to shear and tensile faults in a half-space. *Bulletin of the Seismological Society of America*, *75*(4), 1135–1154. https://doi.org/10.1785/bssa0750041135

Okuwaki, R., Yagi, Y., Taymaz, T., & Hicks, S. P. (2023). Multi-scale rupture growth with alternating directions in a Complex Fault Network during the 2023 South-Eastern Türkiye and Syria earthquake doublet. *Geophysical Research Letters*, *50*(12), e2023GL103480. https://doi.org/10.1029/2023GL103480

Pousse-Beltran, L., Nissen, E., Bergman, E. A., Cambaz, M. D., Gaudreau, É., Karasözen, E., & Tan, F. (2020). The 2020 Mw 6.8 Elazığ (Turkey) earthquake reveals rupture behavior of the East Anatolian Fault. *Geophysical Research Letters*, *47*(13), e2020GL088136. https://doi.org/10.1029/2020GL088136

Reilinger, R., McClusky, S., Vernant, P., Lawrence, S., Ergintav, S., Cakmak, R., et al. (2006). GPS constraints on continental deformation in the Africa-Arabia-Eurasia continental collision zone and implications for the dynamics of plate interactions. *Journal of Geophysical Research*, *111*(B5), B05411. https://doi.org/10.1029/2005JB004051

Reitman, N. G., Briggs, R. W., Barnhart, W. D., Hatem, A. E., Thompson Jobe, J. A., DuRoss, C. B., et al. (2023). Rapid surface rupture mapping from satellite data: The 2023 Kahramanmaraş, Turkey (Türkiye), earthquake sequence. *The Seismic Record*, *3*(4), 289–298. https://doi.org/10.1785/0320230029

Scholz, C. H., Dawers, N. H., Yu, J. Z., Anders, M. H., & Cowie, P. A. (1993). Fault growth and fault scaling laws: Preliminary results. *Journal of Geophysical Research*, *98*(B12), 21951–21961. https://doi.org/10.1029/93JB01008

Turkelli, N., Sandvol, E., Zor, E., Gok, R., Bekler, T., Al-Lazki, A., et al. (2003). Seismogenic zones in Eastern Turkey. *Geophysical Research Letters*, *30*(24). https://doi.org/10.1029/2003GL018023

Vanacore, E. A., Taymaz, T., & Saygin, E. (2013). Moho structure of the Anatolian Plate from receiver function analysis. *Geophysical Journal International*, *193*(1), 329–337. https://doi.org/10.1093/gji/ggs107

Wang, K., Zhu, Y., Nissen, E., & Shen, Z.-K. (2021). On the relevance of geodetic deformation rates to earthquake potential. *Geophysical Research Letters*, *48*(11), e2021GL093231. https://doi.org/10.1029/2021GL093231

Wang, X., & Zhan, Z. (2020). Seismotectonics and fault geometries of the 2019 Ridgecrest sequence: Insight from aftershock moment tensor catalog using 3-D Green's functions. *Journal of Geophysical Research: Solid Earth*, *125*(5), e2020JB019577. https://doi.org/10.1029/2020JB019577

Wei, S., Zeng, H., Shi, Q., Liu, J., Luo, H., Hu, W., et al. (2022). Simultaneous rupture propagation through fault bifurcation of the 2021 Mw7.4 Maduo earthquake. *Geophysical Research Letters*, *49*(21), e2022GL100283. https://doi.org/10.1029/2022GL100283

Weiss, J. R., Walters, R. J., Morishita, Y., Wright, T. J., Lazecky, M., Wang, H., et al. (2020). High-resolution surface velocities and strain for Anatolia from Sentinel-1 InSAR and GNSS data. *Geophysical Research Letters*, *47*(17), e2020GL087376. https://doi.org/10.1029/2020GL087376

Wessel, P., Luis, J. F., Uieda, L., Scharroo, R., Wobbe, F., Smith, W. H. F., & Tian, D. (2019). The Generic Mapping Tools Version 6. *Geochemistry, Geophysics, Geosystems*, *20*(11), 5556–5564. https://doi.org/10.1029/2019GC008515

Xu, L., Mohanna, S., Meng, L., Ji, C., Ampuero, J. P., Yunjun, Z., et al. (2023). The overall-subshear and multi-segment rupture of the 2023 Mw7.8 Kahramanmaraş, Turkey earthquake in millennia supercycle. *Communications Earth & Environment*, *4*(1), 379. https://doi.org/10.1038/s43247-023-01030-x

Xu, X., Tong, X., Sandwell, D. T., Milliner, C. W., Dolan, J. F., Hollingsworth, J., et al. (2016). Refining the shallow slip deficit. *Geophysical Journal International*, *204*(3), 1867–1886. https://doi.org/10.1093/gji/ggv563

Zhao, D., Qu, C., Chen, H., Shan, X., Song, X., & Gong, W. (2021). Tectonic and geometric control on fault kinematics of the 2021 Mw7.3 Maduo (China) earthquake inferred from interseismic, coseismic, and postseismic InSAR observations. *Geophysical Research Letters*, *48*(18), e2021GL095417. https://doi.org/10.1029/2021GL095417

References From the Supporting Information

De Zan, F., Prats-Iraola, P., Scheiber, R., & Rucci, A. (2014). Interferometry with TOPS: Coregistration and azimuth shifts. In *Paper presented at EUSAR 2014; 10th European conference on synthetic aperture radar*. VDE.

Fattahi, H., Agram, P., & Simons, M. (2016). A network-based enhanced spectral diversity approach for TOPS time-series analysis. *IEEE Transactions on Geoscience and Remote Sensing*, *55*(2), 777–786. https://doi.org/10.1109/tgrs.2016.2614925

Goldstein, R. M., & Werner, C. L. (1998). Radar interferogram filtering for geophysical applications. *Geophysical Research Letters*, *25*(21), 4035–4038. https://doi.org/10.1029/1998gl900033

Liang, C., & Fielding, E. J. (2017a). Interferometry with ALOS-2 full-aperture ScanSAR data. *IEEE Transactions on Geoscience and Remote Sensing*, *55*(5), 2739–2750. https://doi.org/10.1109/tgrs.2017.2653190

Liang, C., & Fielding, E. J. (2017b). Measuring azimuth deformation with L-band ALOS-2 ScanSAR Interferometry. *IEEE Transactions on Geoscience and Remote Sensing*, *55*(5), 2725–2738. https://doi.org/10.1109/tgrs.2017.2653186

Luo, H., Li, Z., Chen, J., Pearson, C., Wang, M., Lv, W., & Ding, H. (2019). Integration of Range Split Spectrum Interferometry and conventional InSAR to monitor large gradient surface displacements. *International Journal of Applied Earth Observation and Geoinformation*, *74*, 130–137. https://doi.org/10.1016/j.jag.2018.09.004

Ma, Z. F., Jiang, M., & Huang, T. (2020). A sequential approach for Sentinel-1 TOPS time-series co-registration over low coherence scenarios. *IEEE Transactions on Geoscience and Remote Sensing*, *1*, 1–9.

Ma, Z. F., Jiang, M., Khoshmanesh, M., & Cheng, X. (2021). Time series phase unwrapping based on graph theory and compressed sensing. *IEEE Transactions on Geoscience and Remote Sensing*, *60*, 1–12. https://doi.org/10.1109/tgrs.2021.3066784

Rosu, A.-M., Pierrot-Deseilligny, M., Delorme, A., Binet, R., & Klinger, Y. (2015). Measurement of ground displacement from optical satellite image correlation using the free open-source software MicMac. *ISPRS Journal of Photogrammetry and Remote Sensing*, *100*, 48–59. https://doi.org/10.1016/j.isprsjprs.2014.03.002

Rupnik, E., Daakir, M., & Pierrot Deseilligny, M. (2017). MicMac – A free, open-source solution for photogrammetry. *Open Geospatial Data, Software and Standards*, *2*(1), 14. https://doi.org/10.1186/s40965-017-0027-2

Stumpf, A., Michéa, D., & Malet, J.-P. (2018). Improved co-registration of Sentinel-2 and Landsat-8 imagery for Earth surface motion measurements. *Remote Sensing*, *10*(2), 160. https://doi.org/10.3390/rs10020160